Research Square

Preprints are preliminary reports that have not undergone peer review.
They should not be considered conclusive, used to inform clinical practice,
or referenced by the media as validated information.

Mixed Layer Salinity Seesaw in the Eastern Tropical Indian Ocean: Mechanism Revisited and Regulation to the Indonesian throughflow

Jingwen Chen

mc45217@um.edu.mo

University of Macau https://orcid.org/0009-0009-2252-022X

Qin-Yan Liu

South China Sea Institute of Oceanology Chinese Academy of Sciences https://orcid.org/0000-0001-5244-6993

Yuhong Zhang

South China Sea Institute of Oceanology Chinese Academy of Sciences

Xiuquan Wan

Ocean University of China

Ningning Zhang

Nanjing University of Information Science and Technology

Jinyu Shang

South China Sea Institute of Oceanology Chinese Academy of Sciences

Yong Cao

Ocean University of China

Research Article

Keywords: Salinity seesaw, ETIO, ENSO, amplified salinity contribution

Posted Date: June 23rd, 2026

DOI: https://doi.org/10.21203/rs.3.rs-9893492/v1

License: This work is licensed under a Creative Commons Attribution 4.0 International License.
Read Full License

Mixed Layer Salinity Seesaw in the Eastern Tropical Indian Ocean: Mechanism Revisited and Regulation to the Indonesian throughflow

Jingwen Chen[12], Qin-Yan Liu[134*], Yuhong Zhang[5], Xiuquan Wan[6], Ningning Zhang[7], Jinyu Shang[134], Yong Cao[6]

Co-first author: Qin-Yan Liu

[1]China-Sri Lanka Belt and Road Joint Laboratory on Tropical Oceanography, South China Sea Institute of Oceanology, Chinese Academy of Sciences, Guangzhou, P. R. China

[2]Faculty of Science and Technology, Smart Ocean Technology, University of Macau, Macau, P. R. China

[3]Laboratory of Tropical Oceanography, South China Sea Institute of Oceanology, Chinese Academy of Sciences, Guangzhou, P. R. China

[4]University of Chinese Academy of Sciences, Beijing 100049, R. R. China

[5]State Key Laboratory of Tropical Oceanography, South China Sea Institute of Oceanology, Chinese Academy of Sciences, Guangzhou, P. R. China

[6]State Key Laboratory of Physical Oceanography, Ocean University of China, Qingdao, P. R. China

[7]School of Marine Sciences, Nanjing University of Information Science and Technology, Nanjing, China

*Corresponding author: Qin-Yan Liu, email: qyliu66@scsio.ac.cn. South China Sea Institute of Oceanology, Chinese Academy of Sciences, Guangzhou, P. R. China

Abstract:

Ocean salinity regulates global overturning circulation, yet the remote impacts from El Niño-Southern Oscillation (ENSO) on eastern tropical Indian Ocean (ETIO) salinity variability and its contribution to the Indonesian Throughflow (ITF) transport remain poorly quantified. Using Argo observational data, this study investigates the interannual variability of mixed layer salinity (MLS) in ETIO and its underlying mechanisms, focusing on two dynamically critical regions that regulate the ITF transport: the Downstream Buoyant Pool (DBP) and the equatorial eastern Indian Ocean (EEIO). Results reveal a robust seesaw in MLS anomalies between two regions (fresher in DBP vs. saltier in EEIO), with ENSO as the primary driver and Indian Ocean Dipole (IOD) as a secondary modulator. Salinity budget analysis reveals contrasting controls: DBP dominated by freshwater flux (FWF; advection (ADV) second), EEIO dominated by ADV (FWF second), plus vertical entrainment. During El Niño, positive evaporation-minus-precipitation (E-P) and rainfall deficits drive DBP salinification, whereas anomalous southeasterly winds shoal the mixed layer depth (MLD) and drive westward advection, freshening the EEIO—the opposite occurs during La Niña. Salinity variations in the two regions significantly modulate the ITF: the halosteric component explains 35.71% of interannual variance, and its contribution is significantly amplified during ENSO events, especially during El Niño with above ~82% alone, in contrast to IOD events where temperature dominates. These findings fundamentally advance understanding of salinity dynamics in key oceanic circulation regions.

Keywords: Salinity seesaw, ETIO, ENSO, amplified salinity contribution.

1. Introduction

Understanding ocean salinity is key to elucidating a wide range of marine processes, including ocean circulation, ecological distributions, and climate regulation. In the eastern tropical Indian Ocean (ETIO), salinity variations act as a critical "climate switch" influencing equatorial dynamics and cross-basin exchanges (Yu, 2011; Du et al., 2015). More broadly, ocean salinity regulates global overturning circulation by modulating density gradients that drive thermohaline processes (Lagerloef, 2002). One prominent example is the Indonesian Throughflow (ITF)—the sole low-latitude gateway connecting the Pacific and Indian Oceans (Gordon, 2005)—whose strength and structure are potentially influenced by salinity variations in the ETIO (Andersson and Stigebrandt, 2005).

As shown in Fig. 1, the ETIO presents a pronounced low-salinity belt along Sumatra's coast (9°S-15°S) with significant interannual variability, consistent with previous studies (Vinayachandran and Nanjundiah, 2009; Grunseich et al., 2011; Nyadjro and Subrahmanyam, 2014; Du and Zhang, 2015). Atmospheric freshwater fluxes (evaporation-minus-precipitation, E-P), dominated by precipitation, are the major factor controlling this climatological pattern (Yu, 2011). Both freshwater forcing and ocean dynamics contribute to the strong salinity variability in this region (Fig. 1b, Rao and Sivakumar, 2003).

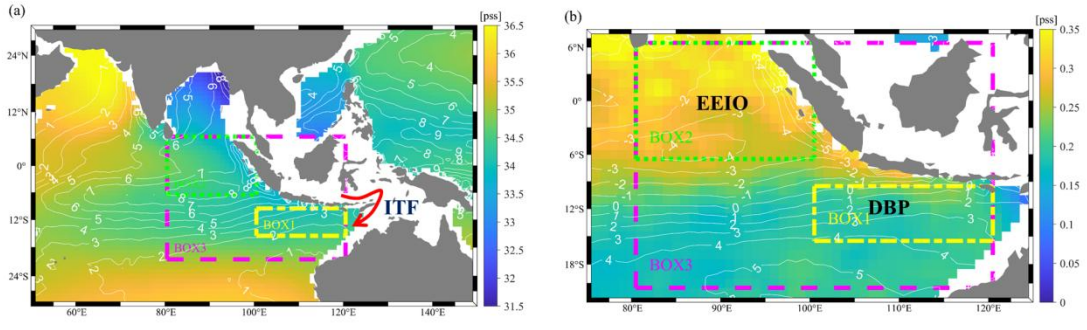


Fig. 1 (a) Climatological mean of mix layer salinity (MLS) (color; unit: pss) and precipitation (white contours; unit: mm·day^{-1}); (b) the standard deviation of MLS (color)

and climatological mean of E-P (white contours; unit: mm·day^{-1}). For convenience, the Downstream Buoyant Pool (DBP; 9°S–15°S, 100°E–120°E) is defined as Box1, the equatorial eastern Indian Ocean (EEIO; 6°N–6°S, 80°E–100°E) as Box2, and the Eastern Tropical Indian Ocean (ETIO, encompassing both DBP and EEIO) as Box3. ITF transport can be determined by the steric difference between DBP and EEIO, according to the method of AS05.

Indian Ocean Dipole (IOD, Saji et al., 1999) and El Niño–Southern Oscillation (ENSO) are the two dominant climate modes influencing salinity variations in this region (e.g., Masson et al., 2004; Phillips et al., 2005; Thompson et al., 2006; Durack and Wijffels, 2010; Grunseich et al., 2011; Du et al., 2015; Feng et al., 2015; N. Zhang et al., 2016; Y. Zhang et al., 2013; 2016; 2018; Köhler et al., 2018; Kido et al., 2019a; 2019b; Nie et al., 2020; Z. Zhang et al., 2022). For instance, during positive IOD events, positive salinity anomalies occur along the Sumatra coast, with opposite pattern during negative IOD events (Masson et al., 2004; Thompson et al., 2006; Grunseich et al., 2011). These anomalies are primarily controlled by oceanic zonal current (Y. Zhang et al., 2013; Chi et al., 2021). Furthermore, Y Zhang et al. (2016) identified a sea surface salinity dipole mode (S-IOD) in the ETIO, which matures in November—December, lagging two months behind the IOD, and exhibits a longer duration, persisting until September—October of the following year. They further pointed out that, on interannual timescales, the S-IOD is primarily driven by equatorial salinity advection associated with wind anomalies and net freshwater flux anomalies in the southeastern tropical Indian Ocean.

ENSO signals drive salinity variability in the Indian Ocean by altering atmospheric forcing and ocean processes via wave dynamics (Godfrey, 1996; Potemra, 1999; 2005; Wijffels and Meyers, 2004). Their influence is manifested through changes in precipitation (Gordon et al., 2012), wind-driven Ekman transport, and delayed salinity responses due to oceanic memory effects (Ren and Riser, 2009). Furthermore, the

100 “freshwater plug” mechanism in the Makassar Strait (Gordon et al., 2003; 2012)
101 exhibits pronounced interannual variability and subsequently influences Indian Ocean
102 salinity by modulating ITF transport, which is tightly linked to ENSO-forced freshwater
103 transport changes (Lu et al., 2023).

104 Salinity variability in the ETIO critically regulate ITF transport by modulating the
105 pressure gradient between two key regions (see Fig. 1): the Downstream Buoyant Pool
106 (DBP; 9°S-15°S, 100°E-120°E) and equatorial eastern Indian Ocean (EEIO; 6°N-6°S,
107 80°E-100°E) (Andersson and Stigebrandt, 2005, hereafter AS05). The salinity accounts
108 for 36 ± 7% of interannual ITF variability (Hu and Sprintall, 2016), and its contribution
109 is expected to increase under global warming due to intensified hydrological cycles
110 (Guo et al., 2023; Lu et al., 2024).

111 While many studies have addressed salinity variability in the ETIO, the specific
112 mechanisms through which ENSO influences the basin-scale salinity patterns are still
113 not well resolved. In particular, given the recognized importance of the DBP and EEIO
114 in regulating ITF dynamics, it is essential to further investigate the regional salinity
115 characteristics and their quantitative contribution to ITF transport. This study aims to
116 (1) revisit the interannual salinity variability in the ETIO, with a focus on the DBP and
117 EEIO regions, using mixed layer budget analysis; and (2) quantify the thermosteric and
118 halosteric contributions to ITF transport following the AS05 method. Our findings
119 indicate that the mix layer salinity (MLS) anomalies display a seesaw mode between
120 the DBP and EEIO. While this pattern is analogous to the S-IOD described by Y. Zhang
121 et al. (2016), its underlying mechanism is governed by ENSO rather than the IOD.
122 Meanwhile, we found that salinity contribution amplifies during ENSO events (~82%
123 during independent El Niño), contrasting with IOD events where temperature
124 contribution dominates.

125 The remainder of this paper is organized as follows. Section 2 describes the
126 datasets and methodologies used in this study. Section 3 examines the interannual
127 variability of MLS anomaly in ETIO, with a focus on the DBP and EEIO regions;
128 elucidates the associated mechanisms during ENSO events; and analyzes the

thermosteric and halosteric contributions to ITF transport anomalies. The possible role of IOD is discussed in Section 4, and Section 5 provides a summary.

2. Data and Methods

2.1 Data description

a. Argo datasets

Monthly mean BOA Argo datasets were obtained from the China Argo Real-time Data Center (National Marine Environmental Forecasting Center, China). The data have a spatial resolution of 1°×1° (covering 60°S to 60°N) and a vertical resolution of 58 pressure levels from 0 to 2000 dbar (see dataset documentation for full list), spanning January 2004 to present. The dataset includes temperature (T), salinity (S), mixed layer depth (MLD), isothermal layer depth, and composite mixed layer depth, derived from over 1.8 million quality-controlled Argo profiles. The MLS was derived through vertical averaging of the S profiles within the BOA Argo dataset, constrained by the defined MLD.

b. Ocean currents product

Monthly mean zonal and meridional ocean current components were derived from the ECMWF Ocean Reanalysis System 5 (ORAS5), which has a horizontal resolution of approximately 0.25°×0.25° and a vertical resolution of 75 levels (ranging from the surface to ~5500 m depth), covering the global ocean. The dataset assimilates observations from multiple sources, including Argo floats, satellite altimetry, and XBT profiles, and spans from January 1958 to the present.

c. Other datasets

Monthly 10-m zonal and meridional wind components, evaporation (E) and total precipitation (P) were derived from the ECMWF Reanalysis v5 (ERA5) dataset, with a spatial resolution of 0.25°×0.25°, spanning from January 1950 to present (Hersbach et al., 2023). The Niño3.4 index and the Dipole Mode Index (DMI) were obtained from NOAA. Geostrophic transport from XBT measurements in the upper 400 m (Liu et al.,

2015) was used for comparison with the AS05-based ITF transport. All products were anomaly-calculated by removing their 2004–2024 climatological means.

2.2 MLS budget analysis

The MLS budget equation (Feng et al., 1998) can be expressed as:

$$\frac{\partial S}{\partial t} = -\left(u\frac{\partial S}{\partial x} + v\frac{\partial S}{\partial y}\right) - \frac{S_0(P-E)}{h} - w_e\frac{S-S_{-h}}{h} + \varepsilon \qquad (1a)$$

$$w_e = \frac{\partial h}{\partial t} + \left(\frac{\partial hu}{\partial x} + \frac{\partial hv}{\partial y}\right) \qquad (1b)$$

where, S is MLS; t denotes the time; S_0 is the Sea Surface Salinity (SSS); S_{-h} is the salinity at bottom of the mixed layer; u and v are the zonal and meridional ocean currents velocities of the mixed layer; P and E are the precipitation and evaporation; the w_e is the vertical entrainment velocity; h is MLD, and the ε is the residual term, including unresolved processes such diffusive and other term errors.

To explore interannual variability, the variables can be divided into climatological seasonal cycles and interannual variations, such as $S = \bar{S} + S'$, where $\bar{S}$ is the climatologically seasonal cycle, and S' is the interannual variations. By ignoring higher-order nonlinear terms, the disturbance equation can be rewritten (Y. Zhang et al., 2013) as:

$$\underbrace{\frac{\partial S'}{\partial t}}_{St} = \underbrace{-\left(\bar{u}\frac{\partial S'}{\partial x} + u'\frac{\partial \bar{S}}{\partial x} + \bar{v}\frac{\partial S'}{\partial y} + v'\frac{\partial \bar{S}}{\partial y}\right)}_{ADV} \underbrace{-\frac{\overline{S_0}(P-E)'}{h}}_{FWF} \underbrace{-{w_e}'\frac{\overline{(S-S_{-h})}}{h}}_{Vertical} + \underbrace{\varepsilon}_{residual} \qquad (2)$$

In Eq. (2), from left to right, the terms are the MLS tendency (St), horizontal advection (ADV), surface freshwater forcing (FWF), vertical entrainment forcing (hereinafter referred to as vertical), and residual terms, respectively. The horizontal advection term contains two parts, one is the effect of mean salinity gradient advected by the anomalous currents $-u'\frac{\partial \bar{S}}{\partial x}$, $-v'\frac{\partial \bar{S}}{\partial y}$ (denoted as $Adv_{x(u')}$, $Adv_{y(v')}$ respectively), and the second is the anomalous salinity gradient advected by the mean currents $-\bar{u}\frac{\partial S'}{\partial x}$, $-\bar{v}\frac{\partial S'}{\partial y}$ (denoted as $Adv_{x(s')}$, $Adv_{y(s')}$ respectively).

2.3 ITF transport diagnoses

The ITF transport can be calculated based on AS05 according to the following formula:

$$Q_\lambda = \frac{g\Delta\rho H^2}{2f(\lambda)\rho_0} \qquad (3a)$$

$$ITF = Q_{\lambda_N} - Q_{\lambda_S} \qquad (3b)$$

where g is the acceleration of gravity, $f(\lambda)$ is the Coriolis parameter, H is the penetration depth of DBP (refer to the setting of $H = 1200\,m$ in AS05), ρ_0 is the reference density at 1200 m, $\Delta\rho$ is the density difference between DBP and EEIO (as shown in Fig. 1b), λ_N and λ_S are latitudes at north and south boundaries of DBP (λ_N =10°S, λ_S =16°S), respectively. Here, a positive ITF means the water from the Pacific Ocean entering the Indian Ocean.

Consistent with Hu and Sprintall (2016), the density ρ of seawater is calculated by the formula given as a function of T and S (Fofonoff and Millard, 1983):

$$\rho(S,T,0) = \rho_w + (b_0 + b_1T + b_2T^2 + b_3T^3 + b_4T^4)S + (c_0 + c_1T + c_2T^2)S^{\frac{3}{2}} + d_0S^2 \qquad (4)$$

$$\rho_w = a_0 + a_1T + a_2T^2 + a_3T^3 + a_4T^4 + a_5T^5 \qquad (5)$$

where $a_{i=0,..5}$, $b_{i=0,..4}$, $c_{i=0,..2}$ and d_0 are constants (see Table 1).

To separate the ITF halosteric effect (ITF_S) and thermosteric effect (ITF_T), the halosteric effect density ρ_S and the thermosteric effect density ρ_T are calculated respectively. Namely

$$\rho_S = \rho(S,\bar{T}) \qquad \rho_T = \rho(\bar{S},T)$$

$$ITF_S = ITF(S,\bar{T}) \qquad ITF_T = ITF(\bar{S},T)$$

Among them, $\bar{T}$ and $\bar{S}$ are the climatological average of T and S, respectively.

Lastly, to quantify the relative contribution of thermosteric (ITF'_T) and halosteric components (ITF'_S) to ITF anomaly (ITF'), the absolute values (Pi) of ITF'_S and ITF'_T are calculated as a percentage of the total variation (Hu and Sprintall, 2016):

$$P_i = \frac{|ITF'_i|}{|ITF'_S|+|ITF'_T|+|ITF'_R|} \times 100\% \qquad (6)$$

where i is T or S, $ITF'_R = ITF' - ITF'_S - ITF'_T$ is the residual term, and $|*|$ denotes

the absolute value.

Table 1 Constants for the International Equation of State of Seawater.

PARAMETERS	VALUE
a_0	$+999.842594$
a_1	$+6.793952 \times 10^{-2}$
a_2	-9.095290×10^{-3}
a_3	$+1.001685 \times 10^{-4}$
a_4	-1.120083×10^{-6}
a_5	$+6.536332 \times 10^{-9}$
b_0	$+8.24493 \times 10^{-1}$
b_1	-4.0899×10^{-3}
b_2	$+7.6438 \times 10^{-5}$
b_3	-8.2467×10^{-7}
b_4	$+5.3875 \times 10^{-9}$
c_0	-5.72466×10^{-3}
c_1	$+1.0227 \times 10^{-4}$
c_2	-1.6546×10^{-6}
d_0	$+4.8314 \times 10^{-4}$

2.4 ENSO/IOD events classification

If the 3-month moving average of the Niño3.4 index reaches or exceeds an

absolute value of 0.5 and persists for at least 5 months, it is regarded as an ENSO event; when the absolute value of the DMI index reaches or exceeds the standard deviation of the DMI index from 2004 to 2024 and persists for at least 3 months, it is regarded as an IOD event. Following this classification, there are six El Niño events (2004/2005, 2006/2007, 2009/2010, 2014-2016, 2018/2019 and 2023/2024), seven La Niña events (2007/2008, 2008/2009, 2010/2011, 2011/2012, 2017/2018, 2020/2021 and 2021/2022), seven positive IOD events (2006, 2012, 2015, 2017, 2018/2019, 2019 and 2023), and three negative IOD events (2005, 2016 and 2022). The details of duration and persistence of ENSO and IOD events are given in Table 2, 3 respectively. The 2019 positive IOD was the strongest event since the 1960s which developed independently without coinciding El Niño (Du et al., 2020).

Table 2 Years identified as ENSO events.

YEAR	ENSO	DURATION (MONTHS)	START
2004	El Niño	6	Aug.
2006	El Niño	5	Sept.
2007	La Niña	10	Aug.
2008	La Niña	5	Nov.
2009	El Niño	9	Jul.
2010	La Niña	12	Jun.
2011	La Niña	7	Aug.
2014	El Niño	20	Oct.
2017	La Niña	6	Oct.

2018	El Niño	9	Oct.
2020	La Niña	8	Sept.
2021	La Niña	18	Sept.
2023	El Niño	13	May.

Table 3 Years identified as IOD events.

YEAR	IOD	ENSO PHASE	DURATION (MONTHS)	START
2005	Negative	-	4	Aug.
2006	Positive	El Niño	3	Sept.
2012	Positive	-	3	Jul.
2015	Positive	El Niño	5	Jul.
2016	Negative	-	6	Jun.
2017	Positive	-	5	Mar.
2018	Positive	El Niño	6	Sept.
2019	Positive	El Niño	9	Apr.
2022	Negative	La Niña	3	Sept.
2023	Positive	El Niño	14	Mar.

2.5 EOF and partial correlation analysis

Empirical Orthogonal Function (EOF) analysis, also known as Principal Component Analysis (PCA), extracts dominant spatiotemporal patterns from geophysical data by decomposing a space-time field into orthogonal modes, each

comprising a spatial pattern (EOF) and a corresponding time series (principal component, PC). The first mode explains the maximum fraction of the total variance. In this study, EOF is applied to MLS anomaly field to capture its leading mode, which represents interannual variability.

Partial correlation analysis quantifies the linear relationship between two variables while controlling for the effect of one or more additional variables (Cai et al., 2012). In this study, partial correlation analysis is employed to examine the independent relationship between MLS anomalies and climate indices (e.g., Niño3.4 and DMI) by removing the mutual influence of ENSO and IOD, thereby identifying the specific imprint of each mode on salinity variability.

3. Results

3.1 Interannual variability of the MLS anomalies

3.1.1 The MLS anomalies averaged in DBP and EEIO

Fig. 2 shows the time series of MLS anomalies averaged over DBP (Box1) and EEIO (Box2), respectively, together with the salinity anomaly profiles in the upper 300 m. The results reveal that the MLS anomalies in the DBP and EEIO exhibit a robust out-of-phase relationship, with a zero-lag correlation coefficient of -0.44. That is, high salinity in Box1 coincided with low salinity in Box2 from mid-2006 to 2008, with the opposite relationship from 2008 to 2011—a seesaw behavior that was most pronounced during the 2015/2016 El Niño. Vertical profiles show that these salinity anomalies are largely restricted to the upper 100 m (Fig. 2b-c), unlike temperature anomalies, which frequently extend below 200 m (not shown)—underscoring the distinct dynamics that govern them (Qu and Meyers, 2005). The analysis reveals that these MLS anomalies are primarily influenced by ENSO, which will be discussed in Section 3.1.2.

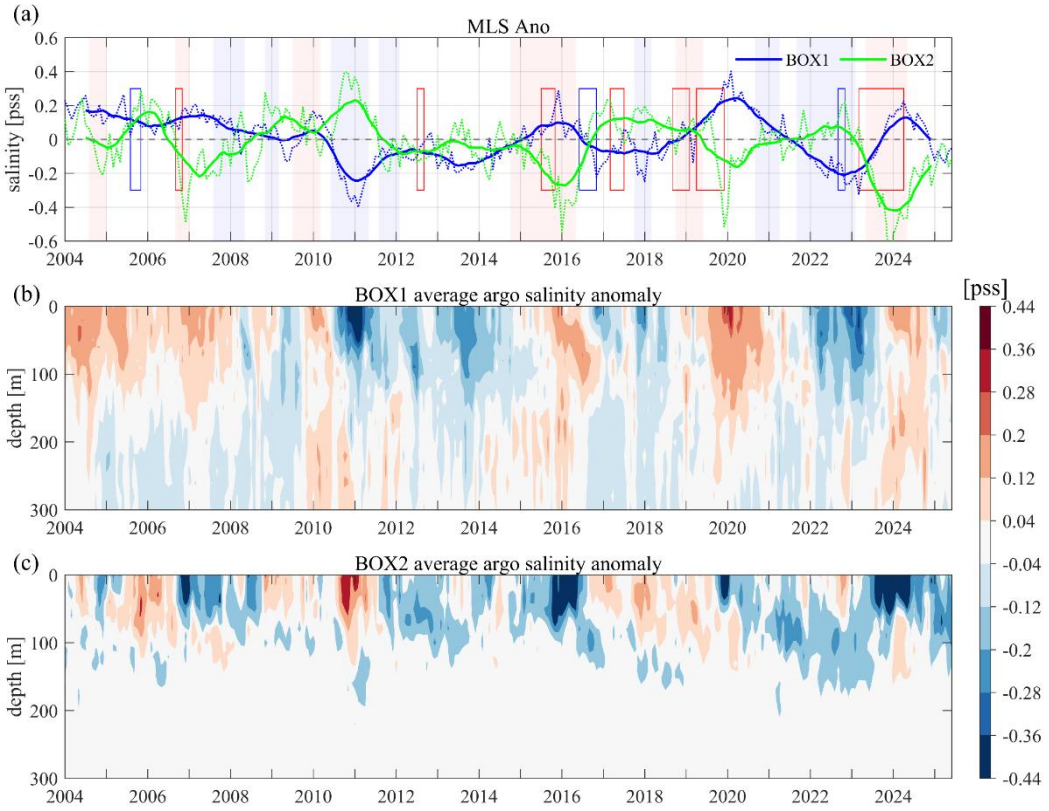


Fig. 2 (a) Time series of MLS anomalies (unit: pss) averaged over Box1 and Box2, respectively (dashed lines: original data; solid lines: after a 13-point running mean). (b, c) Vertical profiles of salinity anomalies in Box1 (b) and Box2 (c), respectively. In (a), the red (blue) shaded area represents the El Niño events (La Niña events). The red (blue) box area represents positive IOD events (negative IOD events).

3.1.2 ENSO-dominated MLS seesaw mode: EOF analysis

Through EOF analysis, we find that EOF mode 1 accounts for 37.15% of the total variance of the first five modes (Fig. 3a), revealing a distinct MLS seesaw mode in the ETIO. Its spatial distribution aligns with the locations of Box1 (DBP) and Box2 (EEIO), with positive values centered over the DBP and negative values centered over the EEIO. Box1 MLS anomaly is strongly positively correlated with PC1 ($r = 0.77$), whereas Box2 MLS anomaly shows a strong negative correlation ($r = -0.82$).

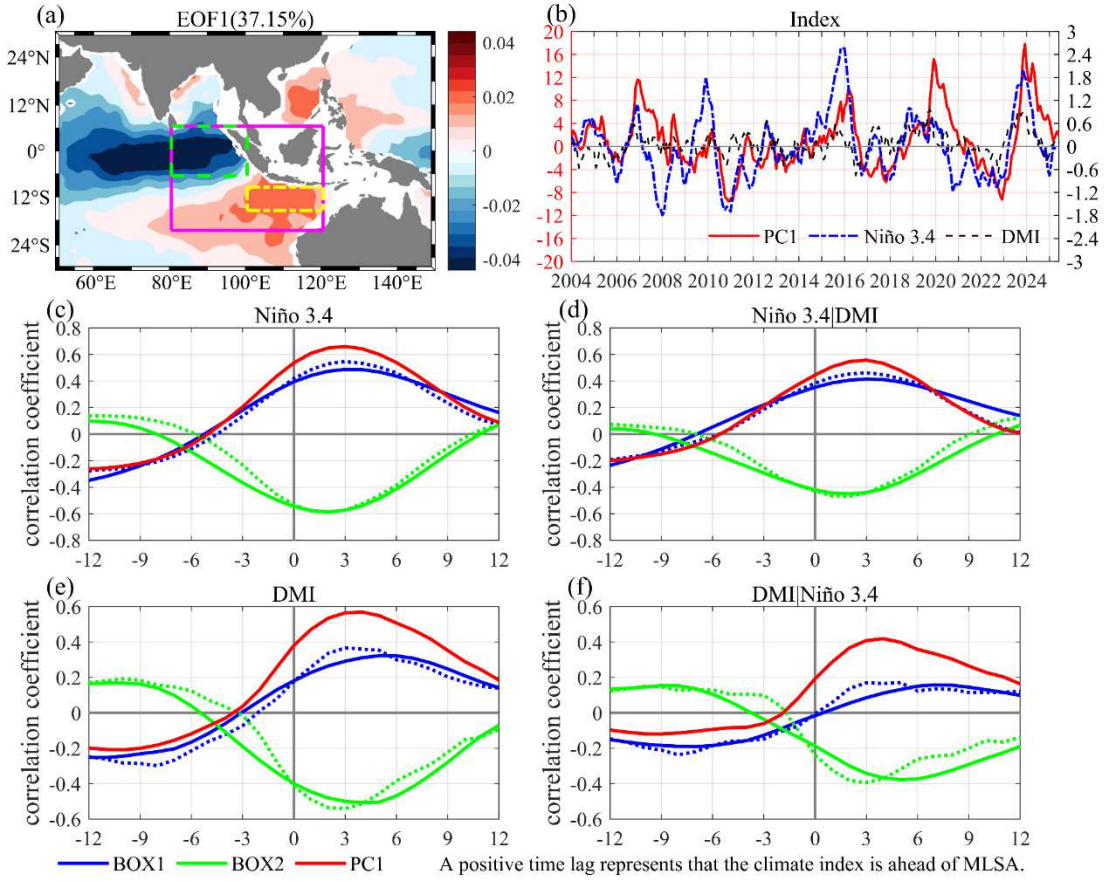


Fig. 3 (a) Spatial pattern of EOF1 of MLS anomalies. (b) PC1, Niño3.4 index and DMI index. (c) Lead lag correlations between the Niño3.4 index and Box1 MLS anomaly (blue), Box2 MLS anomaly (green), and PC1 (red). (d) Lead lag partial correlations between the Niño3.4 index and the same variables after removing the linear influence of the DMI. (e) Similar to (c), but for the correlation with the DMI. (f) Similar to (d), but for the partial correlation with the DMI after removing the linear influence of the Niño3.4. In (c-f), dashed lines denote raw correlations, and solid lines represent correlations after a 13 month running mean filter. Positive lags indicate that the climate index leads MLS anomaly.

Correlation analysis reveals that PC1 (Fig. 3b) is positively correlated with the Niño3.4 index, with a correlation coefficient of 0.66 when Niño3.4 leads PC1 by three months (Fig. 3c). Box1 MLS anomaly exhibits its strongest positive correlation with

the Niño3.4 index at a lag of three months (r = 0.49, Fig. 3c), whereas Box2 shows a maximum negative correlation at a lag of two months (r = –0.58, Fig. 3c). After removing the influence of the IOD, the correlation between PC1 and Niño3.4 index remains high (r=0.56 at a three-month lag, Fig. 3d). Furthermore, while PC1 is also significantly correlated with the DMI (r = 0.57 at a four-month lag, Fig. 3e), this correlation drops markedly once the effect of ENSO is removed (r = 0.42 at a four-month lag, Fig. 3f). Partial correlation analysis confirms that the MLS seesaw mode is dominated by ENSO, with IOD playing a secondary modulating role. Fig. 3e-f reveals that only Box2 (EEIO) correlates strongly with the IOD, suggesting that the IOD primarily modulates salinity in this region via local dynamical anomalies (further discussed in Section 4).

Above analysis shows that the salinity seesaw pattern existing in ETIO between EEIO and DBP is dominated by ENSO-related signals, where atmospheric forcing (Xie et al., 2002), ocean waveguides via the Indonesian Archipelago (e.g., Wijffels and Meyers, 2004) and ITF transport (Meyers, 1996; England and Huang, 2005; Liu et al., 2015) take effects. Therefore, partial correlation analysis was further employed in Section 3.1.3 to further investigate the impact of ENSO on the MLS anomaly in the ETIO.

3.1.3 Spatial distributions of partial correlation analysis

Fig. 4a-f display the spatial distributions of partial correlation coefficients between MLS anomalies and the Niño3.4 index after removing IOD influence, for lag times of 0, 2, 4, 6, 8 and 10 months (i.e., when MLS anomalies lag Niño3.4 index by these months). Statistical significance was assessed using a two-tailed Student's t-test. After removing the effects of IOD, two main characteristics of MLS anomalies variability related to ENSO events are identified in ETIO. One prominent feature is that the positive correlation signals originating in the western Pacific Ocean propagate into the Indian Ocean through the Indonesian seas (Fig. 4a-f). These signals subsequently

influence the MLS anomalies along the western coast of Australia via Kelvin waves and eventually trigger the westward-propagating Rossby wave. In Box1 (DBP), the maximum positive correlation occurs when MLS anomalies lags Niño3.4 index by two to four months (Fig. 3b-c). The oceanic waveguides processes through the Indonesian Archipelago (Wijffels and Meyers, 2004) play a key role in modulating MLS anomalies variability in the Box1 region. The second characteristic feature is that the negative correlation signal undergoes development and extends westward along the equator, resulting in a significant negative correlation throughout EEIO (Fig. 3a-c, Box2). In the Box2 (EEIO), significant negative correlations are observed when MLS anomalies lag Niño3.4 by two months (Fig. 3b).

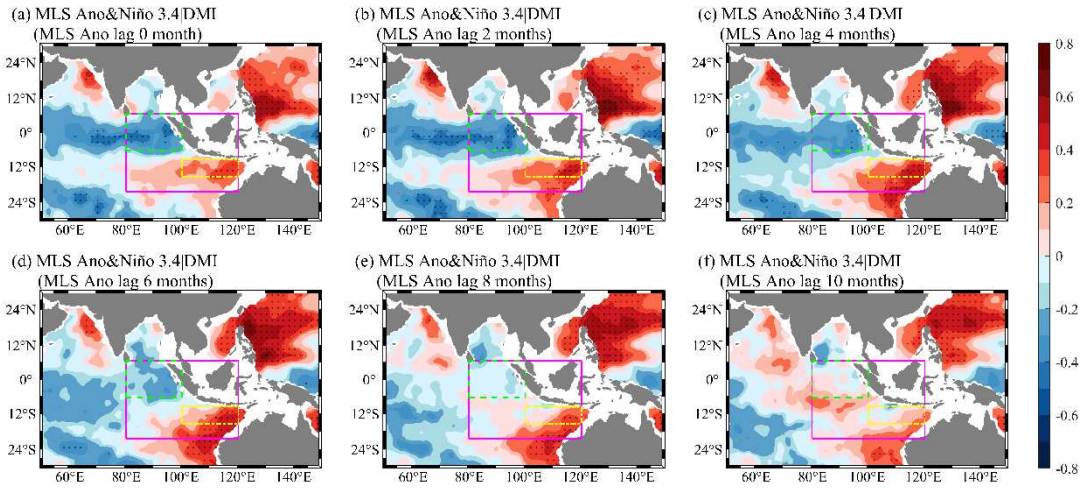


Fig. 4 Spatial distribution of the partial correlation coefficients between Niño3.4 index and MLS anomalies, when MLS anomalies lag by 0 month (a), 2 months (b), 4 months (c), 6 months (d), 8 months (e) and 10 months (f), respectively. Asterisks indicate regions where the correlation passes the t test at the 90% confidence level.

Fig. 4 further reveals that ENSO exerts strong control over mixed layer salinity variability in Indo-Pacific regions. During El Niño (La Niña), saltier (fresher) conditions prevail in the southeastern tropical Indian Ocean (SETIO), driven by a

combination of oceanic advection anomalies and local precipitation changes between 12°S and the northwest coast of Australia (N. Zhang et al., 2016). These conditions correspond to the development of salinity anomalies observed near the eastern Philippine coast (Guan et al., 2019). Consequently, the salinity anomalies in the DBP (Box1) and those near the eastern Philippine coast vary in phase with Niño3.4, exhibiting a simultaneous positive correlation (Fig. 3). Previous studies show that the primary domain of ENSO-related salinity variability spans 13°S–30°S and 100°E–120°E (Nie et al., 2023). However, our results highlight that significant ENSO signals in the equatorial band are mainly confined to 10°S–10°N, 60°E–100°E.

ENSO and IOD often co-occur and interact via Walker circulation modulation (Saji and Yamagata, 2003), complicating Indian Ocean dynamics. Although this MLS seesaw pattern is analogous to the S-IOD described by Y. Zhang et al. (2016), Fig. 3 and Fig. 4 further illustrate that the seesaw pattern in the ETIO—centered over DBP (Box1) and EEIO (Box2) —is predominantly governed by ENSO rather than the IOD. Although IOD-related zonal currents can influence salinity in Box2 (e.g., Grunseich et al., 2011; Z. Zhang et al., 2022), the basin-scale seesaw pattern identified in this study is fundamentally caused by ENSO. This indicate that ENSO-related signals promote the formation and evolution of the salinity seesaw pattern in ETIO, centered around the key regions of DBP and EEIO through atmospheric and oceanic pathways, such as changes in precipitation and ocean advection

3.2. Possible mechanism analysis

3.2.1 Atmospheric and oceanic effects

In this section, composite analysis is conducted to illustrate interannual anomalies associated with El Niño and La Niña events, including ocean currents, E-P, MLD, and winds components (Fig. 5), with two-sample t-tests indicating statistical significance. Here, positive E-P anomalies indicate net freshwater loss from the ocean to the atmosphere, and positive precipitation anomalies denote enhanced rainfall.

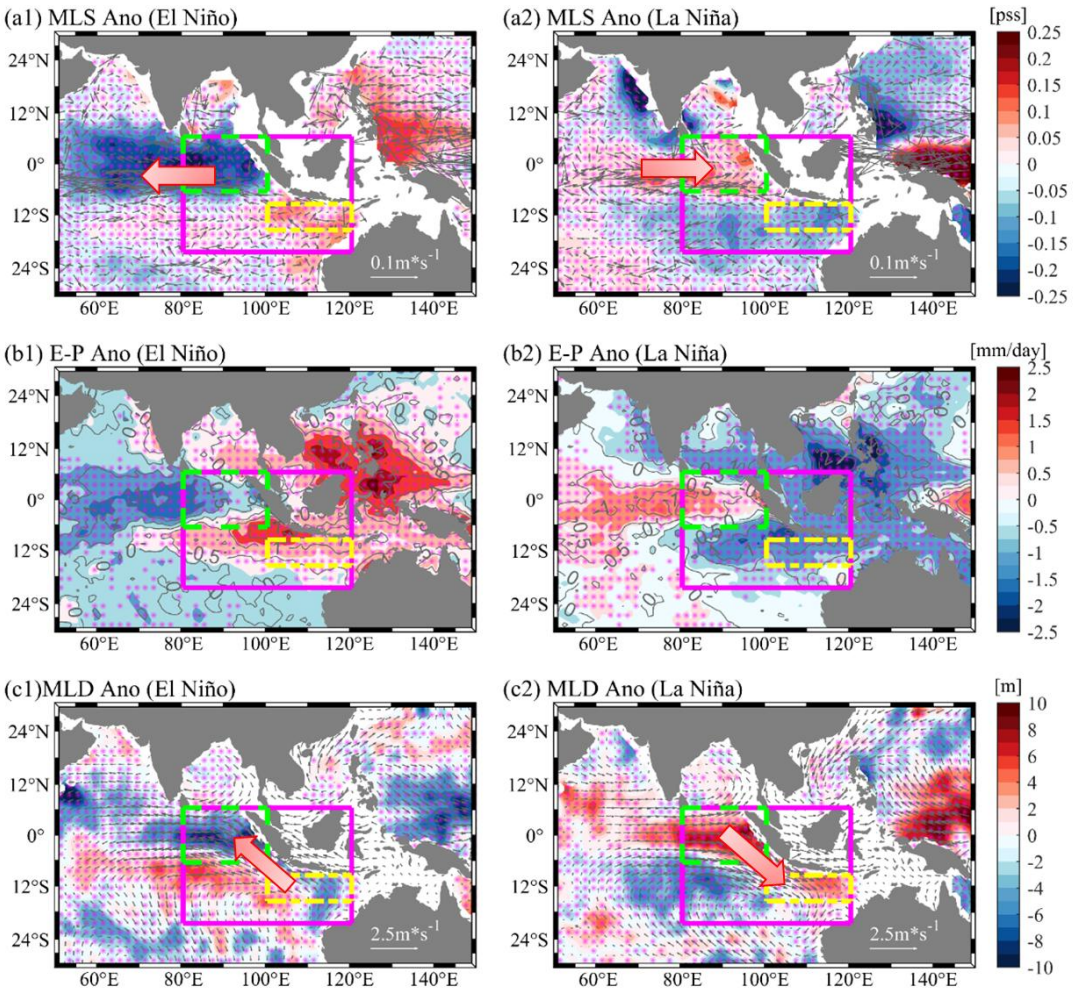


Fig. 5 (a) Composite of MLS (color; unit: pss) and mixed layer velocity anomalies (gray arrows; unit: m·s^{-1}) for El Niño (a1) and La Niña (a2). (b) E P anomalies (color; unit: mm·day^{-1}) and P anomalies (gray contours; unit: mm·day^{-1}) for El Niño (b1) and La Niña (b2). (c) MLD anomalies (color; unit: m) and 10 m wind velocity anomalies (gray arrows; unit: m·s^{-1}) for El Niño (c1) and La Niña (c2). The events of El Niño and La Niña are shown in Table 2. Asterisks indicate areas where the anomalies pass the t-test at the 90% confidence level. The red arrows indicate the anomalous circulation (a1-a2) and the anomalous wind field (c1-c2), respectively. Here, positive MLS anomalies represent saltier conditions, and vice versa for fresher conditions. Positive E-P anomalies indicate that E is greater than P and vice versa indicates that E is less than P.

372 Positive P anomalies represent increased rainfall, and vice versa for decreased rainfall.

373

374 Fig. 5a1 reveals that MLS anomalies in the ETIO display a pronounced east-west
375 seesaw pattern during El Niño. Specifically, increased salinity appears around the ITF
376 outflow region and off the western coast of Australia (centered on DBP region, Box1),
377 while fresher waters extend westward along the equatorial band (12°S–12°N) off
378 Sumatra (centered on the EEIO region). This dominant salinity seesaw reverses during
379 La Niña (Fig. 5a2). Azka and Trilaksono (2024) noted that heavy precipitation over the
380 Indonesian Maritime Continent critically regulates salinity distribution in the
381 surrounding oceans. High salinity in the ITF outflow region stems primarily from
382 reduced maritime continent precipitation (Fig. 5b1). Our analysis confirms that the
383 positive (negative) E-P anomalies and rainfall deficits (surplus) contribute to the
384 anomalously saltier (fresher) conditions in the DBP region during El Niño (La Niña)
385 (Fig. 5b1-b2), underscoring the role of ENSO in large-scale salinity redistribution
386 through atmospheric freshwater fluxes, particularly over the DBP region within ITF
387 outflow.

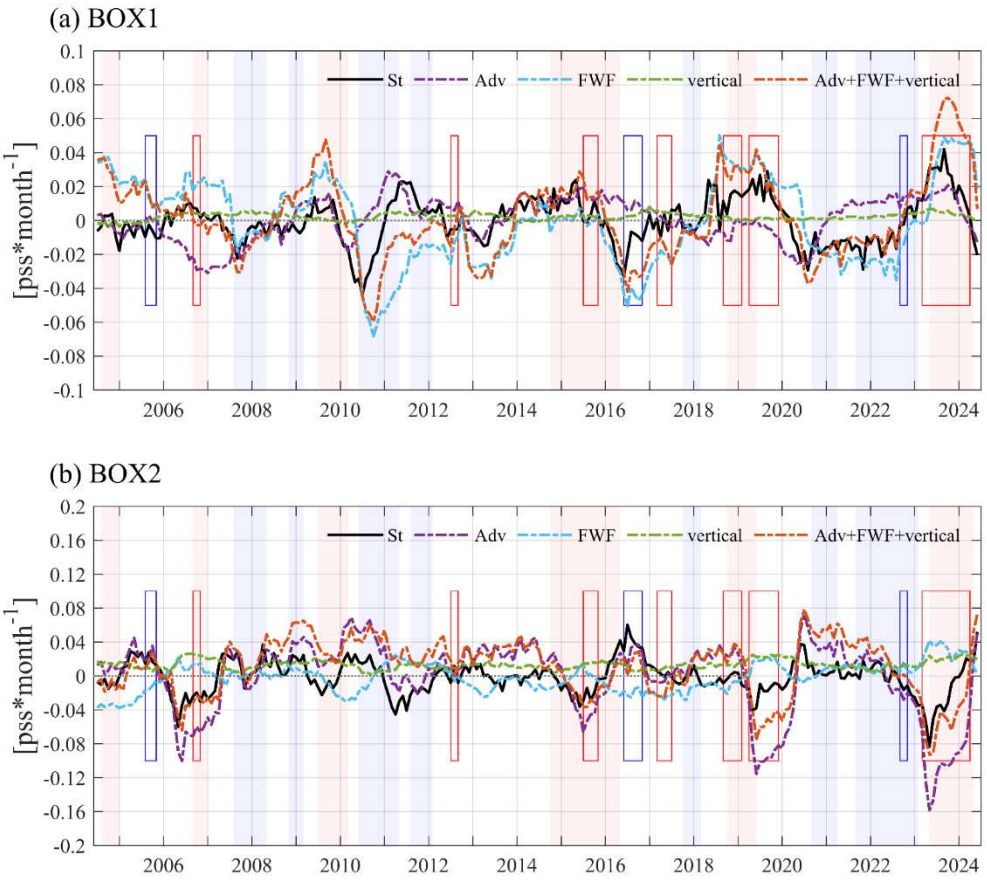
388 However, the salinity anomaly in the EEIO (Box2) is not entirely governed by
389 freshwater flux, particularly along the Sumatra coast, which suggests that the
390 contribution of ocean dynamics should not neglected. The El Niño-driven salinity
391 seesaw involves interacting processes: anomalous southeasterly winds (Fig. 5c1) shoal
392 the MLD in the EEIO (Box2), which is favorable for the freshening induced by negative
393 E-P fluxes (Fig. 5b1). Meanwhile, abnormally ocean currents advect diluted waters
394 westward, reinforcing the equatorial salinity minimum (Fig. 5a1). During La Niña
395 events, anomalous northwesterly winds (Fig. 5c2) induce abnormal eastward currents
396 (Fig. 5a2) and deepen the MLD along Sumatra's coast (Fig. 5c2). There is a prominent
397 barrier layer in the EEIO region, so changes in the mixed layer alone cannot directly
398 reflect the vertical salinity transport. Here, wind-driven shoaling (deepening) of the
399 mixed layer often corresponds to strengthening (weakening) of upwelling transport.

Under these conditions, both fresher and saltier salinity anomalies tend to occur in the EEIO during ENSO events (Sprintall and Tomczak, 1992; Z. Zhang et al., 2022).

The qualitative analysis highlights that ENSO controls the salinity variability in Box1 (DBP) and Box2 (EEIO) through distinct processes, thereby governing the formation and development of salinity seesaw pattern (Fig. 5). Thus, atmospheric freshwater fluxes and oceanic advection and mixing jointly shape regional salinity patterns, characterized with distinct responses—El Niño-driven salinification in Box1 and El Niño-modulated freshening in Box2—that underpin the observed salinity seesaw.

3.2.2 Salinity budget analysis

The salinity budget balance enables a quantitative diagnosis of the contribution of various processes to salinity variations in the study regions. After applying a 13-point running mean, the correlation coefficients between MLS tendency and surface freshwater forcing, as well as horizontal advection in Box1, are 0.47 and 0.24, respectively. Budget analysis indicates that on interannual timescales, surface freshwater forcing serves as the primary driver of MLS tendency in Box1, while horizontal advection plays a secondary role (Fig. 6a). In EEIO (Box2), both surface freshwater forcing and horizontal advection significantly influence the MLS tendency (Fig. 6b), with correlation coefficients of -0.49 and 0.66, respectively. This indicates that horizontal advection is the dominant regulator of MLS tendency in Box2, consistent with previous studies emphasizing the primacy of oceanic processes in salinity variability (Durack and Wijffels, 2010), whereas surface freshwater forcing acts to dampen salinity changes. Further investigation reveals that vertical entrainment demonstrates minimal impact in Box1 ($r = 0.14$) but exhibits a comparatively stronger influence in Box2 ($r = -0.24$).



425

426 **Fig. 6** Time series of the MLS anomalies budget after applying a 13-point running mean
427 (unit: pss·month^{-1}). A negative salinity tendency indicates freshening, and a negative
428 freshwater flux corresponds to net precipitation input.

429

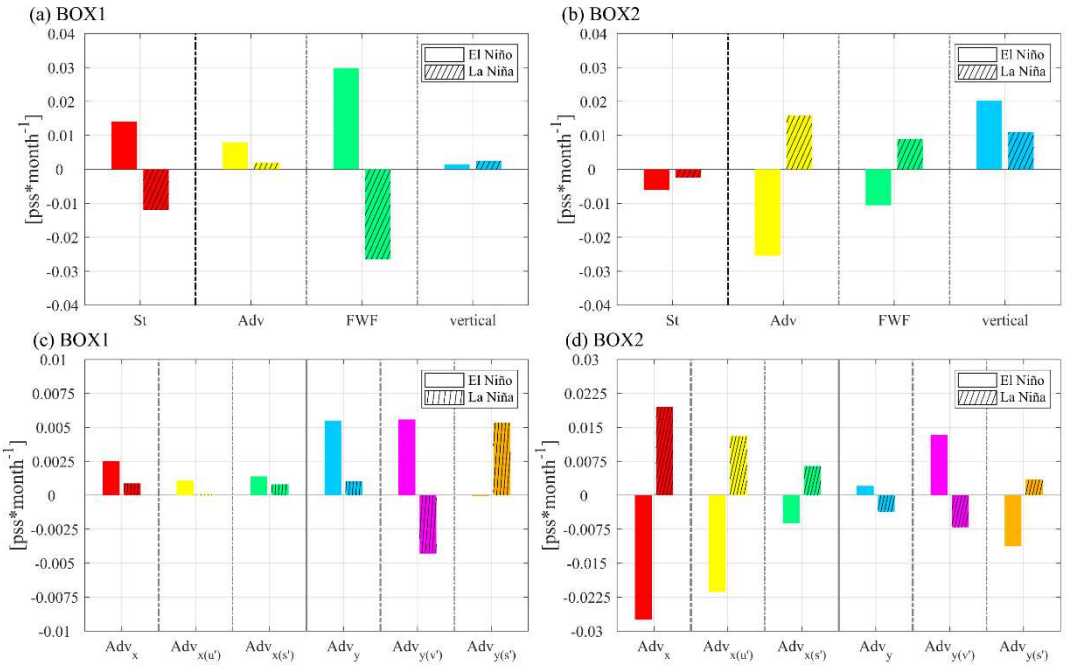


Fig. 7 (a, b) Averaged salinity budget terms and subitems during El Niño and La Niña. (c, d) Averaged horizontal advection terms during El Niño and La Niña. Unit: pss·month^{-1}.

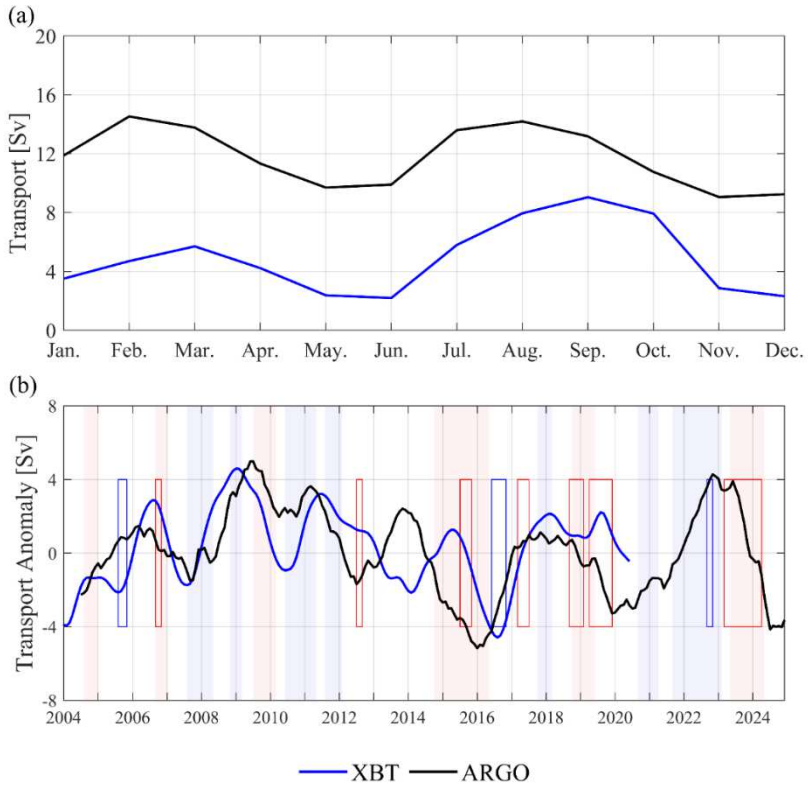
To further elucidate the mechanisms underlying this distinct seesaw pattern between the two regions (DBP and EEIO), which is primarily related to atmospheric and oceanic processes (Santoso et al., 2017), Fig. 7 presents a composite analysis of salinity budget during ENSO events. The results show that MLS anomalies averaged over Box1 are significantly larger than those in Box2 (Fig. 7a, b). El Niño drives positive salinity anomalies in Box1, whereas La Niña events yields negative salinity anomalies. It further confirms that the MLS tendency in Box1 is dominated by surface freshwater forcing, with horizontal advection as secondary factor and vertical entrainment being negligible (Fig. 7a). In contrast, Box2 exhibits negative MLS anomalies during both El Niño and La Niña events (Fig. 7b). In this region, the role of horizontal advection is more important than that of freshwater flux, and vertical entrainment also contributes substantially to MLS variability (Fig. 7b). Further analysis

shows that horizontal advection (comprising velocity variation and salinity gradient terms) dominates Box2 salinity variability during ENSO events. Pronounced meridional and zonal salt advection, driven primarily by velocity changes (Fig. 7c, d), align with prior dynamical findings (Feng et al., 2015).

3.3 The salinity contribution to ITF during ENSO events

3.3.1 Separated thermosteric and halosteric components

We applied the AS05 method to estimate ITF transport using Argo data. Fig. 8 compares the ITF transport time series derived from our Argo-based diagnosis and geostrophic transport from XBT observations (updated from Liu et al., 2015). Our Argo-based calculation incorporated a 1200 m bathymetric constraint, whereas the XBT estimates are limited to the upper 400 m. The Argo-based mean ITF transport is 11.76 ± 2.04 Sv. Seasonally, both Argo and XBT records show twin transport peaks in February-March and August-September (Fig. 8a), consistent with Liu et al. (2015), although the Argo estimates lag behind by approximately one month—likely due to differences in spatiotemporal sampling and methods. Of course, although this method can capture some aspects of the seasonal ITF variability, representing deep-channel flows accurately remains a challenge (Feng et al., 2013).



465

466 **Fig. 8** (a) Seasonal cycle of ITF transport (unit: Sv; 1 Sv = 10^6 $m^3 \cdot s^{-1}$): comparison
467 between the diagnosed ITF transport based on the AS05 method using Argo T-S profiles
468 (black line) and the geostrophic ITF transport derived from XBT observations (blue
469 line, Liu et al., 2015). (b) Same as (a) but for ITF transport anomalies after applying a
470 13-point running mean.

471

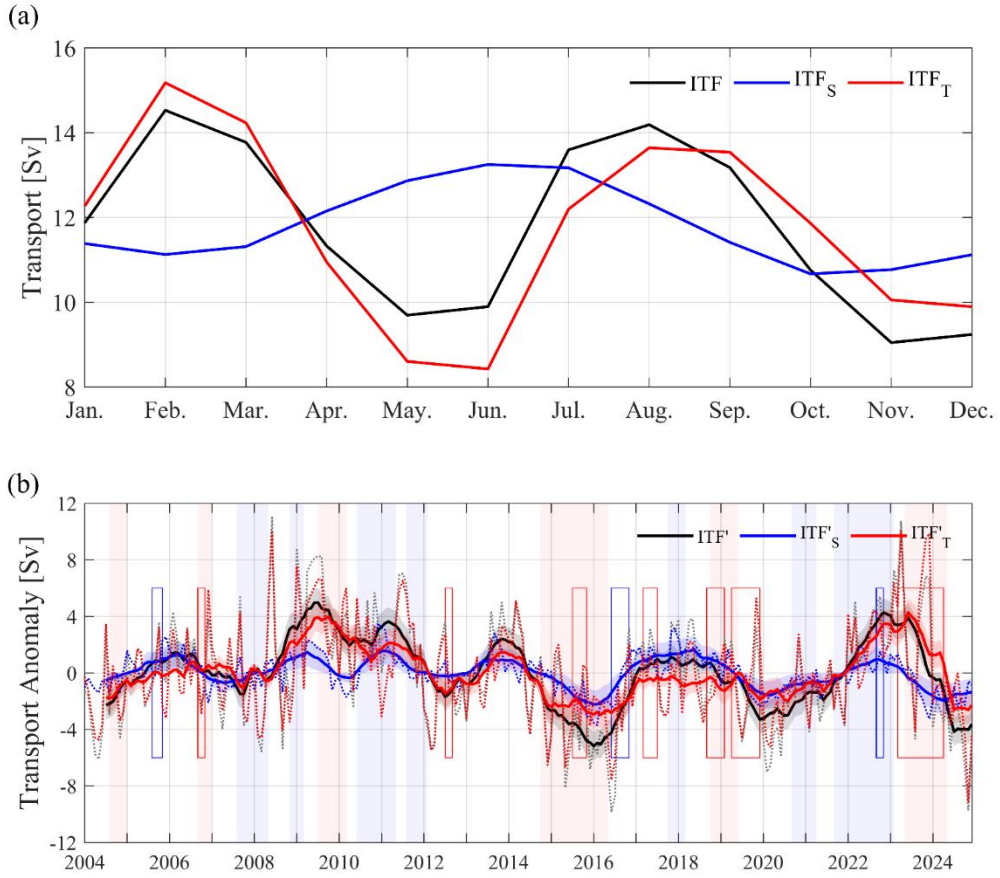


Fig. 9 (a) Monthly climatology of ITF transport and its thermosteric and halosteric components (unit: Sv). (b) Comparison of ITF transport anomalies with its thermosteric and halosteric components. Dashed lines indicate monthly data; solid lines represent the 13-month running mean. The shaded areas in (b) indicate the distribution of the error function.

The ITF transport exhibits strong interannual variability (Fig. 8b), with standard deviations of 2.32 Sv (Argo) and 1.96 Sv (XBT). ITF transport anomalies from Argo and XBT show strong agreement (r = 0.48), supporting the use of the AS05 method and confirming the dynamical importance of the DBP and EEIO regions in regulating ITF variability. This agreement enables further decomposition of thermosteric and halosteric effects on ITF transport (Fig. 9). Both transport estimates (Fig. 8b) correlate

strongly with the Niño3.4 index, with maximum correlations of -0.42 and -0.64 at lags of seven and eight months, respectively (significant at the 95% confidence level). The interannual variability of ITF transport is consistent with previous studies (Meyers, 1996; England and Huang, 2005; Liu et al., 2015): transport weakens during El Niño and strengthens during La Niña, lagging the Niño3.4 index by approximately about seven months.

Based on Hu and Sprintall (2016), component decomposition reveals that the thermosteric component dominates the seasonal ITF cycle, exhibiting semi-annual peaks in February and August (Fig. 9a). The mean transports from the thermosteric and halosteric components are nearly equal: $ITF_T = 11.74 \pm 2.20$ Sv and $ITF_S = 11.80 \pm 0.92$ Sv. The halosteric component modulates seasonality of ITF transport by enhancing transport from April to September and reducing it from November to March, consistent with Liu et al. (2015). On interannual timescales, both ITF'_S and ITF'_T correlate strongly with total ITF' ($r = 0.76$ and 0.93, respectively; Fig. 9b). Their standard deviations are 0.95 Sv and 1.71 Sv, accounting for 35.71% and 64.29% of total ITF interannual variability (2.32 Sv). These results confirm that, while thermosteric effects are dominant, halosteric processes also significantly influence ITF transport (Hu and Sprintall, 2016; Guo et al., 2023).

3.3.2 Composite analysis of ITF transport

Fig. 10 presents the composites of ITF transport and its thermosteric and halosteric components during ENSO and IOD events. Since IOD events can occur either concurrently with ENSO or independently (Baquero-Bernal et al., 2002; Behera and Yamagata, 2003), the results are presented separately in this section for ENSO events with and without co-occurring IOD events. As illustrated in Fig. 10, the averaged ITF transport anomaly decreases by 0.61 Sv during El Niño events and increases by 1.15 Sv during La Niña events (Fig. 10a, b), and ITF'_S exert a stronger influence than ITF'_T (Fig. 10a, b). Based on Fig. 10a-b, the salinity contribution accounts for 51.30% during

La Niña, whereas it becomes the dominant component of the negative ITF anomaly during El Niño (~87.65%). In other words, the salinity contribution is greatly amplified during ENSO events, exceeding that of the temperature contribution.

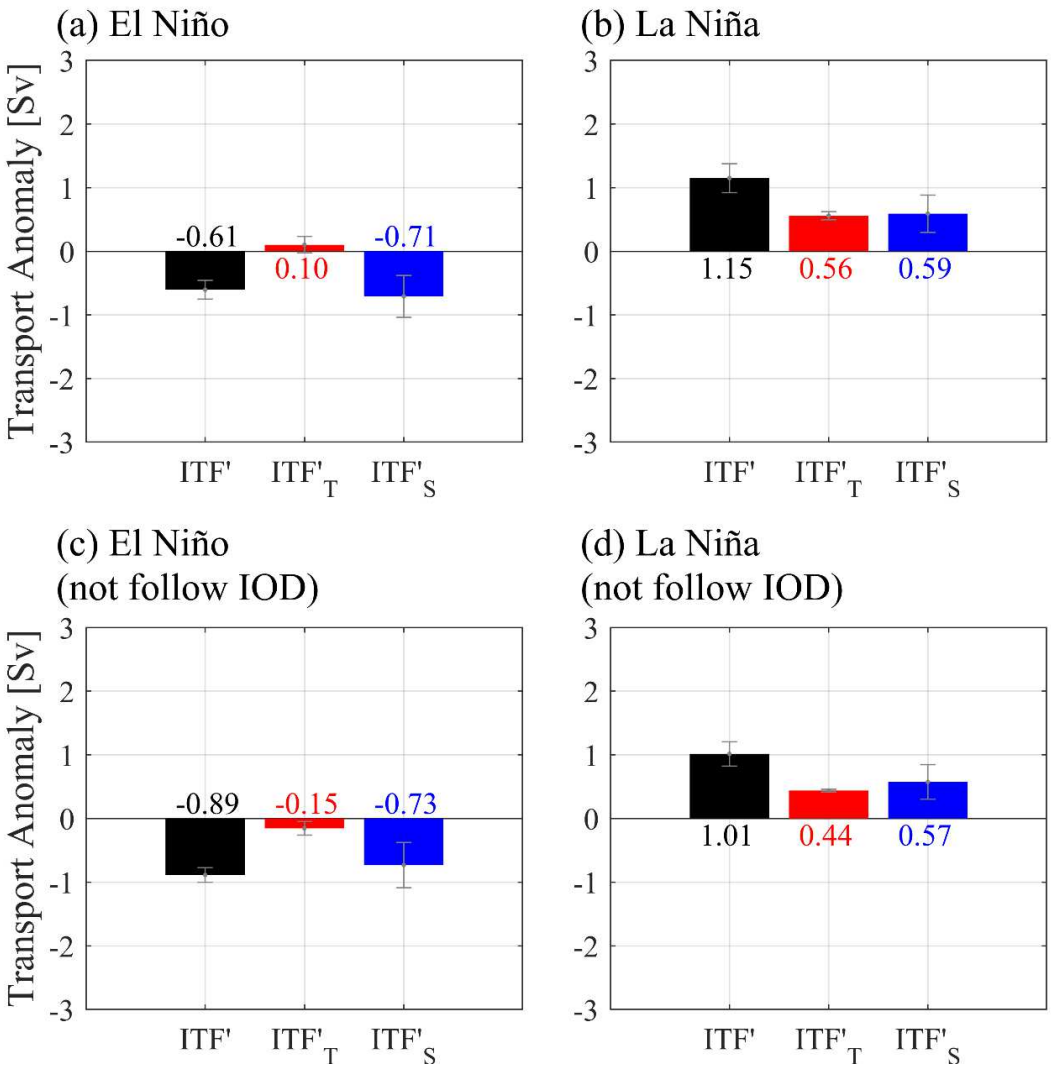


Fig. 10 Averaged ITF transport anomalies and their thermosteric and halosteric components during (a) El Niño, (b) La Niña, (c) El Niño without co-occurring IOD, and (d) La Niña without co-occurring IOD.

Further analysis reveals that when concurrent IOD events are excluded, the ITF

anomaly during El Niño becomes -0.89 Sv, and the salinity contribution still keeps high (approximately 82.02%, Fig. 10c). When co-occurring negative IOD events are excluded, the salinity contribution to the ITF transport during La Niña accounts for approximately 56.44% (Fig. 10d). Although the IOD development can affect ITF transport (Sprintall and Révelard, 2014), the dominant contribution of salinity to ITF transport anomalies during ENSO events is independent of IOD events. This underscores the critical role of salinity in modulating ITF transport under ENSO conditions alone.

4. Discussion

From Fig. 6, we note that the magnitude of MLS tendency in Box2 is substantially larger than that in Box1, with absolute values exceeding 0.04 psu·month^{-1} during specific periods, such as autumn 2005, spring 2006, spring 2011, autumn 2016, and spring 2019. These dates mainly correspond to years with IOD events, during which ENSO events co-occur (Table 3). The co-occurrence of IOD with ENSO can suppress the direct impact of ENSO during its development phase and lead to a delay response to ENSO (Sprintall and Révelard, 2014; Feng et al., 2018; Pujiana et al., 2019). Thus, although this study focuses primarily on the ENSO-related the salinity seesaw pattern and its regulation of the ITF transport, the role of IOD in modulating salinity variability—particularly in the EEIO region—warrants attention. Accordingly, the effects of IOD events are discussed here. Our analysis reveals that IOD events exert a distinct influence on salinity anomalies, often interacting with ENSO to either amplify or dampen their effects.

Similar to Fig. 5, Fig. 11 presents a composite analysis of MLS anomalies, along with corresponding ocean currents and freshwater fluxes. The results indicate that during positive IOD events, salinity anomalies in the EEIO are significantly enhanced, with horizontal advection remaining the dominant driver (Y. Zhang et al., 2013). The anomalous easterly winds characteristic of positive IOD phases strengthens the ocean

currents, promoting the advection of low-salinity waters and leading to pronounced freshening in the equatorial region (Saji and Yamagata, 2003; Thompson et al., 2006). In contrast, negative IOD events are associated with negative E-P anomalies along Sumatra coast and shallower MLD, further complicating the salinity structure in EEIO regions.

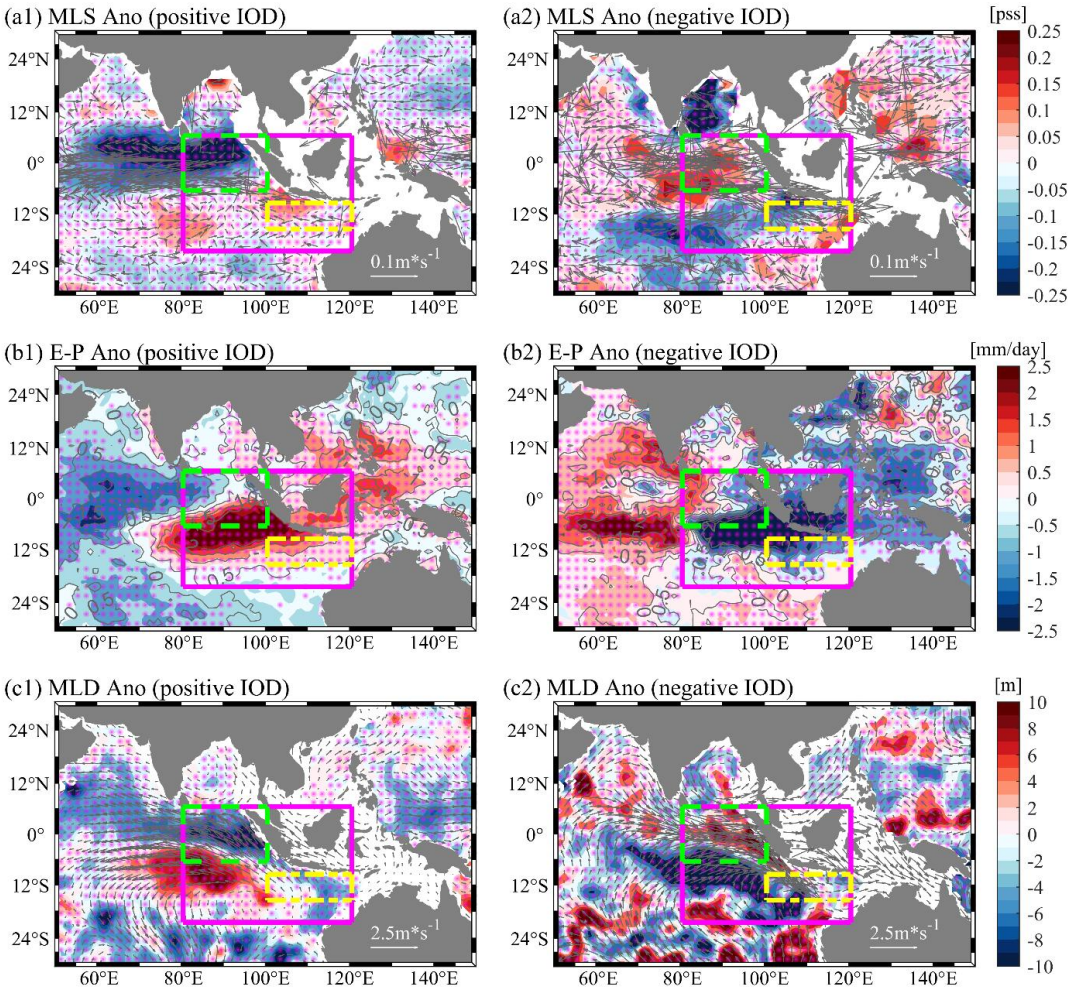


Fig. 11 Similar to Fig. 5, but for IOD events.

Meanwhile, analysis of the contributions of temperature and salinity effects reveals that during IOD events—regardless of whether they occur independently of ENSO

events—the temperature contribution exceeds that of salinity (Fig. 12). While salinity dominates ITF anomalies during ENSO (Fig. 10), temperature plays a more prominent role during IOD events (Fig. 12). This suggests that the physical mechanisms through which IOD influences the ITF are fundamentally different from those of ENSO, likely due to the stronger thermocline modulation and Kelvin wave propagation associated with IOD events (Zhu and Wang, 2024).

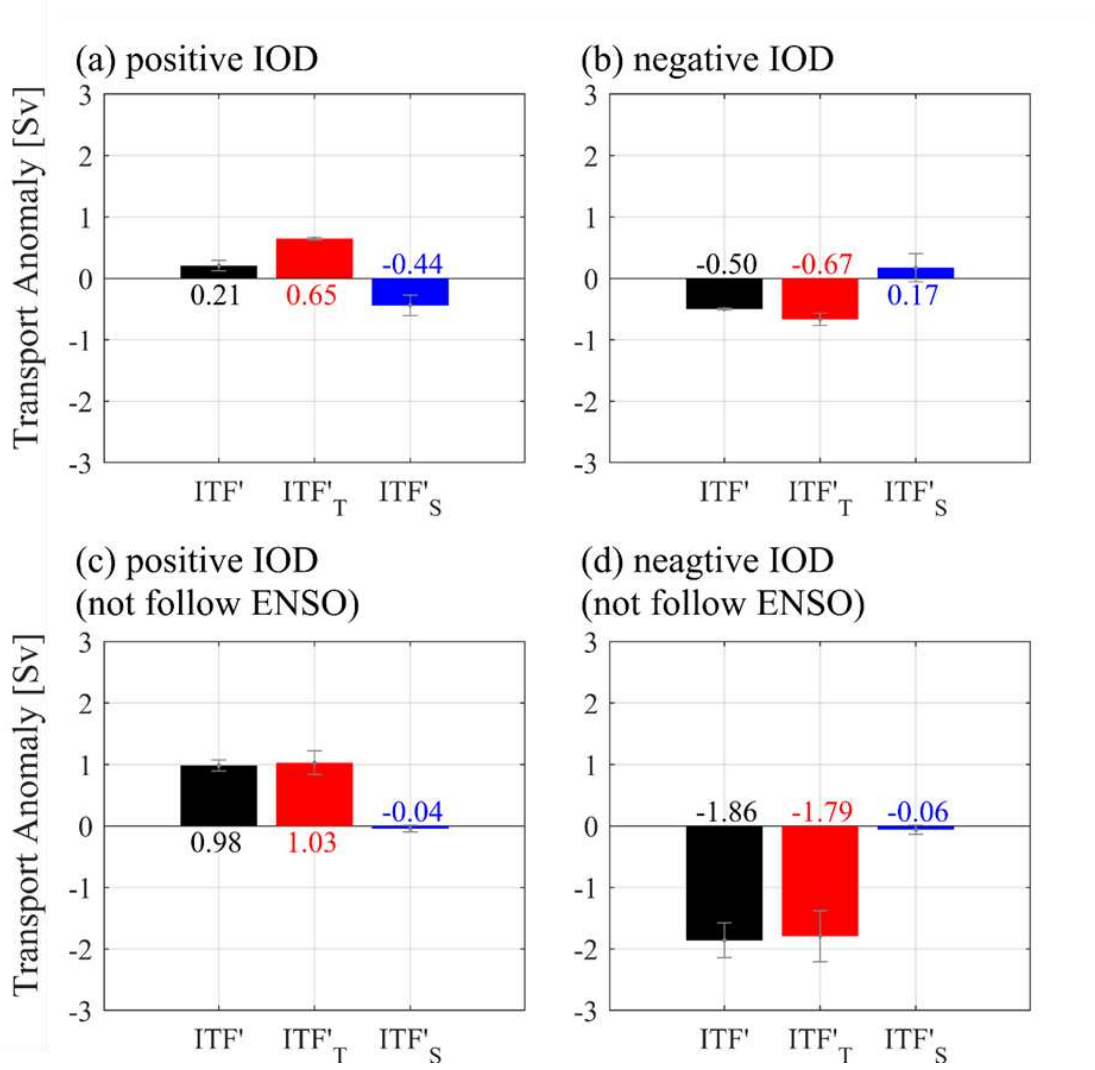


Fig. 12 Similar to Fig. 10, but for IOD events.

5. Summary

570 Using Argo observational data, this study revisits the interannual variability of
571 MLS in the ETIO and its underlying mechanisms, with a focus on two dynamically
572 critical regions that regulate ITF transport: the DBP and the EEIO. The EOF results
573 indicate a significant seesaw pattern in MLS salinity anomalies between the two regions:
574 when the MLS anomaly becomes fresher in the DBP region, it becomes saltier in the
575 EEIO region. This salinity seesaw structure is highly correlated with Niño3.4,
576 indicating that ENSO events are the primary factor driving its occurrence, while the
577 role of IOD is secondary.

578 Salinity budget analysis indicates that: in the Box1 (DBP) region, FWF is the most
579 important term, followed by ADV; in the Box2 (EEIO) region, ADV is the most
580 important term, followed by FWF, and of course, vertical entrainment also plays a
581 certain regulating role. The ENSO-driven salinity seesaw is controlled by atmospheric
582 freshwater fluxes in the DBP region, but by wind-modulated ocean advection, mixed
583 layer depth, and vertical mixing in the EEIO. Specifically, during El Niño, positive E–
584 P anomalies and rainfall deficits dominate DBP salinification, while ocean dynamics
585 prevail in freshening the EEIO—anomalous southeasterly winds shoal the mixed layer
586 and drive westward advection (See the mechanism schematic diagram, Fig. 13). The
587 opposite occurs during La Niña. The IOD modulates this salinity seesaw primarily in
588 the EEIO region, where co-occurring IOD events amplify ENSO's influence (Yang et
589 al., 2007; L. Zhang et al., 2021), potentially through the capacitor effects (Xie et al.,
590 2009).

591

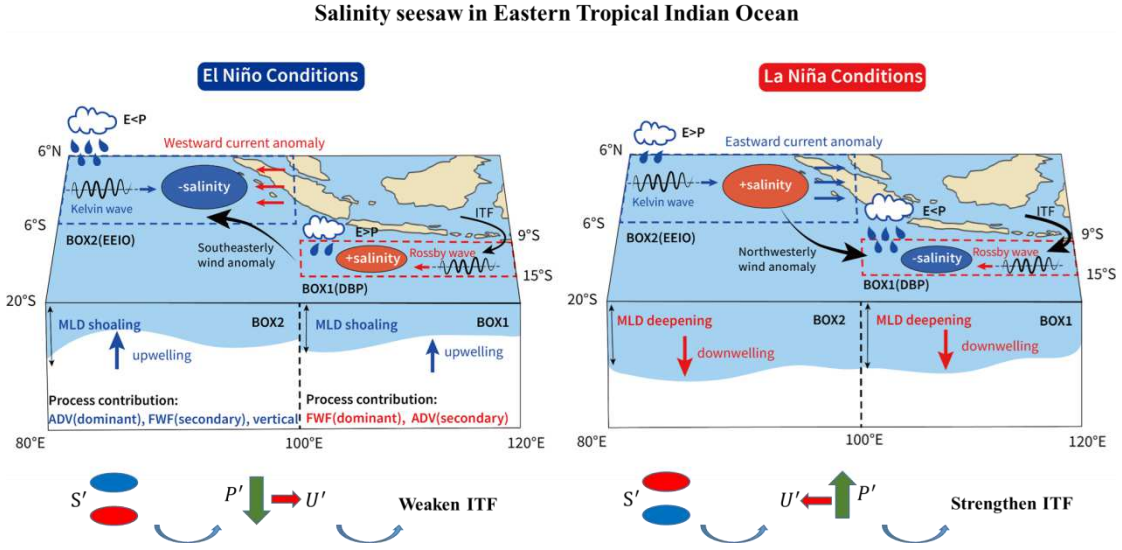


Fig. 13 Schematic diagram of the mechanism for the salinity seesaw structure between DBP and EEIO in the ETIO region during ENSO events. By establishing an anomalous southward (or northward) pressure gradient, the seesaw mode of salinity anomalies acts to weaken (or strengthen) the ITF transport during El Niño (or La Niña) conditions.

Salinity changes in the DBP and EEIO significantly modulate the ITF. The halosteric component modulates ITF seasonally (enhancing Apr–Sep, reducing Nov–Mar) and explains 35.71% of interannual variance, confirming its significant role alongside dominant thermosteric effects. Furthermore, the salinity contribution is found to be amplified during ENSO events, and its importance for the ITF transport does not depend on IOD influences. However, the temperature contribution is more pronounced for IOD events. These results provide critical insights into the contrasting physical processes between the two regions and demonstrate that ENSO plays a key role in generating abnormal dipole-like salinity variations, thus fundamentally advancing our understanding of salinity dynamics in regions that govern oceanic circulation (Hu and Sprintall, 2017), under the global warming background with more frequent ENSO events (Cai et al., 2021).

Acknowledgements: This work was jointly supported by the National Natural Science Foundation of China (Grant 42176027, 42276007, 41876017, 41576012). The authors also appreciated the contributions of High-Performance Computing Division and HPC managers Zhou WEI and Dandan SUI of the South China Sea Institute of Oceanology, Chinese Academy of Sciences. The authors gratefully acknowledge the provision of the reanalysis and in-situ observational datasets used in this study. We sincerely thank the European Centre for Medium-Range Weather Forecasts (ECMWF) for providing the ORAS5 ocean reanalysis data and the ERA5 monthly reanalysis data (specifically the 10-meter wind components, evaporation, and total precipitation). We also extend our appreciation to the International Argo Program and the China Argo Real-time Data Center for making the BOA-Argo gridded product (temperature, salinity, and mixed layer depth) publicly available. Their efforts in maintaining and sharing these high-quality climate datasets have been crucial to this research.

Data Availability Statement:

The datasets used in this study are publicly available:

- BOA Argo data: China Argo Real-time Data Center (National Marine Environmental Forecasting Center, China; http://www.argo.org.cn/), covering January 2004–June 2025.

-ERA5 wind components, evaporation, and precipitation: Copernicus Climate Change Service (C3S) Climate Data Store (CDS; https://cds.climate.copernicus.eu/datasets/reanalysis-era5-single-levels-monthly-means?tab=overview/), January 1950 – present.

- ORAS5 ocean current components (u and v): Copernicus Climate Change Service (C3S) Climate Data Store (CDS; https://cds.climate.copernicus.eu/datasets/reanalysis-oras5?tab=overview), January 1958 – present.

All scripts for analysis are available from the corresponding author upon request.

Competing Interests: The authors declare no competing interests.

Funding: This work is funded by the National Natural Science Foundation of China 624 (Grant 42176027, 42276007, 41876017, 41576012)

Authors' contributions: Qin-Yan Liu supervised this research and offered constructive guidance on the study design and manuscript preparation. Jingwen Chen conducted all analyses, prepared Figs. 1-12, and drafted the manuscript. Jinyu Shang provided assistance in generating Fig. 13. All authors made substantially contributions to the writing and subsequent revision of the manuscript.

References:

Andersson HC, Stigebrandt A (2005) Regulation of the Indonesian throughflow by baroclinic draining of the North Australian Basin. Deep Sea Research Part I: Oceanographic Research Papers 52:2214–2233. https://doi.org/10.1016/j.dsr.2005.06.014

Azka MA, Trilaksono NJ (2024) Comparative Analysis of Diurnal and Seasonal Variations in Precipitation of Mesoscale Convective System and Non-Mesoscale Convective System over Borneo Island. Jurnal Meteorologi dan Geofisika 25:83–92. https://doi.org/10.31172/jmg.v25i2.1101

Baquero-Bernal A, Latif M, Legutke S (2002) On Dipole like Variability of Sea Surface Temperature in the Tropical Indian Ocean. J Climate 15:1358–1368. https://doi.org/10.1175/1520-0442(2002)015%253C1358:ODVOSS%253E2.0.CO;2

Behera SK, Yamagata T (2003) Influence of the Indian Ocean Dipole on the Southern Oscillation. Journal of the Meteorological Society of Japan Ser II 81:169–177. https://doi.org/10.2151/jmsj.81.169

Cai W, Van Rensch P, Cowan T, Hendon HH (2012) An Asymmetry in the IOD and ENSO Teleconnection Pathway and Its Impact on Australian Climate. Journal of Climate 25:6318–6329. https://doi.org/10.1175/JCLI-D-11-00501.1

664 Cai, W., Santoso, A., Collins, M. et al (2021). Changing El Niño–Southern Oscillation
665 in a warming climate. Nat Rev Earth Environ 2, 628–644.
666 https://doi.org/10.1038/s43017-021-00199-z

667 Chi N-H, Lien R-C, D'Asaro EA (2021) The Mixed Layer Salinity Budget in the
668 Central Equatorial Indian Ocean. Journal of Geophysical Research: Oceans
669 126:e2021JC017280. https://doi.org/10.1029/2021JC017280

670 C3S (Copernicus Climate Change Service) (2019) Ocean reanalysis product.
671 C3S_ERA5LAND_ORAS5. Centre for Environmental Data Analysis.
672 https://dx.doi.org/10.24381/cds.8667b3f7. Accessed 2026

673 Du Y, Zhang Y (2015) Satellite and Argo Observed Surface Salinity Variations in the
674 Tropical Indian Ocean and Their Association with the Indian Ocean Dipole Mode.
675 Journal of Climate 28:695–713. https://doi.org/10.1175/JCLI-D-14-00435.1

676 Du Y, Zhang Y, Feng M, et al (2015) Decadal trends of the upper ocean salinity in the
677 tropical Indo-Pacific since mid-1990s. Sci Rep 5:16050.
678 https://doi.org/10.1038/srep16050

679 Du Y, Zhang Y, Zhang L-Y, et al (2020) Thermocline Warming Induced Extreme
680 Indian Ocean Dipole in 2019. Geophysical Research Letters 47:e2020GL090079.
681 https://doi.org/10.1029/2020GL090079

682 Durack PJ, Wijffels SE (2010) Fifty-Year Trends in Global Ocean Salinities and Their
683 Relationship to Broad-Scale Warming. Journal of Climate 23:4342–4362.
684 https://doi.org/10.1175/2010JCLI3377.1

685 England MH, Huang F (2005) On the Interannual Variability of the Indonesian
686 Throughflow and Its Linkage with ENSO. Journal of Climate 18:1435–1444.
687 https://doi.org/10.1175/JCLI3322.1

688 Feng M, Benthuysen J, Zhang N, Slawinski D (2015) Freshening anomalies in the
689 Indonesian throughflow and impacts on the Leeuwin Current during 2010–2011.
690 Geophysical Research Letters 42:8555–8562. https://doi.org/10.1002/2015GL065848

691 Feng M, Hacker P, Lukas R (1998) Upper ocean heat and salt balances in response to
692 a westerly wind burst in the western equatorial Pacific during TOGA COARE. J
693 Geophys Res 103:10289–10311. https://doi.org/10.1029/97JC03286

694 Feng M, Zhang N, Qinyan L, Wijffels S (2018) The Indonesian throughflow, its
695 variability and centennial change. Geoscience Letters 5:.
696 https://doi.org/10.1186/s40562-018-0102-2

697 Feng X, Liu H, Wang F, et al (2013) Indonesian Throughflow in an eddy-resolving
698 ocean model. Chin Sci Bull 58:4504–4514. https://doi.org/10.1007/s11434-013-5988-
699 7

700 Fofonoff N, Millard R (1983) Algorithms for Computation of Fundamental Properties
701 of Seawater. UNESCO Tech Pap Mar Sci 44:

702 Godfrey JS (1996) The effect of the Indonesian throughflow on ocean circulation and
703 heat exchange with the atmosphere: A review. Journal of Geophysical Research:
704 Oceans 101:12217–12237. https://doi.org/10.1029/95JC03860

705 Gordon A (2005) Oceanography of the Indonesian Seas and Their Throughflow.
706 oceanog 18:14–27. https://doi.org/10.5670/oceanog.2005.01

707 Gordon AL, Huber BA, Metzger EJ, et al (2012) South China Sea throughflow impact
708 on the Indonesian throughflow: MAKASSAR STRAIT THROUGHFLOW PROFILE.
709 Geophys Res Lett 39:n/a-n/a. https://doi.org/10.1029/2012GL052021

710 Gordon AL, Susanto RD, Vranes K (2003) Cool Indonesian throughflow as a
711 consequence of restricted surface layer flow. Nature 425:824–828.
712 https://doi.org/10.1038/nature02038

713 Grunseich G, Subrahmanyam B, Murty VSN, Giese BS (2011) Sea surface salinity
714 variability during the Indian Ocean Dipole and ENSO events in the tropical Indian
715 Ocean. J Geophys Res 116:2011JC007456. https://doi.org/10.1029/2011JC007456

716 Guan C, Hu S, McPhaden MJ, et al (2019) Dipole Structure of Mixed Layer Salinity in
717 Response to El Niño-La Niña Asymmetry in the Tropical Pacific. Geophysical
718 Research Letters 46:12165–12172. https://doi.org/10.1029/2019GL084817

719 Guo Y, Li Y, Cheng L, et al (2023) An Updated Estimate of the Indonesian
720 Throughflow Geostrophic Transport: Interannual Variability and Salinity Effect.
721 Geophysical Research Letters 50:e2023GL103748.
722 https://doi.org/10.1029/2023GL103748

723 Hersbach H, Bell B, Berrisford P, Biavati G, Horányi A, Muñoz Sabater J, Nicolas J,
724 Peubey C, Radu R, Rozum I, Schepers D, Simmons A, Soci C, Dee D, Thépaut J-N
725 (2020) The ERA5 global reanalysis. Quarterly Journal of the Royal Meteorological
726 Society146(730):1999–2049. https://doi.org/10.1002/qj.3803

727 Hu S, Sprintall J (2016) Interannual Variability of the Indonesian Throughflow: the
728 Salinity Effect. Journal of Geophysical Research: Oceans 121:2596–2615.
729 https://doi.org/10.1002/2015JC011495

730 Hu S, Sprintall J (2017) Observed Strengthening of Inter-basin Exchange via the
731 Indonesian Seas due to Rainfall Intensification. Geophysical Research Letters 44:1448–
732 1456. https://doi.org/10.1002/2016GL072494

733 Kido S, Tozuka T, Han W (2019a) Anatomy of Salinity Anomalies Associated With
734 the Positive Indian Ocean Dipole. J Geophys Res Oceans 124:8116–8139.
735 https://doi.org/10.1029/2019JC015163

736 Kido S, Tozuka T, Han W (2019b) Experimental Assessments on Impacts of Salinity
737 Anomalies on the Positive Indian Ocean Dipole. J Geophys Res Oceans 124:9462–9486.
738 https://doi.org/10.1029/2019JC015479

739 Köhler J, Serra N, Bryan FO, et al (2018) Mechanisms of Mixed-Layer Salinity
740 Seasonal Variability in the Indian Ocean. J Geophys Res Oceans 123:466–496.
741 https://doi.org/10.1002/2017JC013640

742 Lagerloef GSE (2002) Introduction to the special section: The role of surface salinity
743 on upper ocean dynamics, air-sea interaction and climate. J Geophys Res 107:.
744 https://doi.org/10.1029/2002JC001669

745 Li G, Cheng L, Zhu J, Liu C, Guan Y (2017) Building the globally gridded Argo dataset.
746 Journal of Geophysical Research: Oceans122(12):9839–9855.
747 https://doi.org/10.1002/2017JC013018

748 Liu Q, Feng M, Wang D, Wijffels S (2015) Interannual variability of the I ndonesian T
749 hroughflow transport: A revisit based on 30 year expendable bathythermograph data. J
750 Geophys Res Oceans 120:8270–8282. https://doi.org/10.1002/2015JC011351

751 Lu X, Hu S, Guan C, et al (2023) Quantifying the Contribution of Salinity Effect to the
752 Seasonal Variability of the Makassar Strait Throughflow. Geophysical Research Letters
753 50:e2023GL105991. https://doi.org/10.1029/2023GL105991

754 Lu X, Hu S, Sprintall J (2024) The Role of Precipitation and Salinity Effect in
755 Multidecadal Changes and Long-Term Trend of the Indonesian Throughflow. Journal
756 of Climate 37:1317–1331. https://doi.org/10.1175/JCLI-D-23-0248.1

757 Masson S, Boulanger J-P, Menkes C, et al (2004) Impact of salinity on the 1997 Indian
758 Ocean dipole event in a numerical experiment. Journal of Geophysical Research:
759 Oceans 109:. https://doi.org/10.1029/2003JC001807

760 Meyers G (1996) Variation of Indonesian throughflow and the El Niño-Southern
761 Oscillation. J Geophys Res 101:12255–12263. https://doi.org/10.1029/95JC03729

762 Nie X, Liu H, Xu T, Wei Z (2023) Influence of the El Niño-Southern Oscillation on
763 upper-ocean salinity changes in the southeast Indian ocean. Front Mar Sci 10:.
764 https://doi.org/10.3389/fmars.2023.1181278

765 Nie X, Wei Z, Li Y (2020) Decadal Variability in Salinity of the Indian Ocean
766 Subtropical Underwater During the Argo Period. Geophysical Research Letters
767 47:e2020GL089104. https://doi.org/10.1029/2020GL089104

768 Nyadjro ES, Subrahmanyam B (2014) SMOS Mission Reveals the Salinity Structure of
769 the Indian Ocean Dipole. IEEE Geosci Remote Sensing Lett 11:1564–1568.
770 https://doi.org/10.1109/LGRS.2014.2301594

771 Phillips HE, Wijffels SE, Feng M (2005) Interannual variability in the freshwater
772 content of the Indonesian-Australian Basin. Geophysical Research Letters 32:.
773 https://doi.org/10.1029/2004GL021755

774 Potemra J (2005) Indonesian Throughflow Transport Variability Estimated from
775 Satellite Altimetry. oceanog 18:98–107. https://doi.org/10.5670/oceanog.2005.10

776 Potemra JT (1999) Seasonal Variations of Upper Ocean Transport from the Pacific to
777 the Indian Ocean via Indonesian Straits*. J Phys Oceanogr 29:2930–2944.
778 https://doi.org/10.1175/1520-0485(1999)029%253C2930:SVOUOT%253E2.0.CO;2

779 Pujiana K, McPhaden MJ, Gordon AL, Napitu AM (2019) Unprecedented Response of
780 Indonesian Throughflow to Anomalous Indo-Pacific Climatic Forcing in 2016. J
781 Geophys Res Oceans 124:3737–3754. https://doi.org/10.1029/2018JC014574

782 Qu T, Meyers G (2005) Seasonal variation of barrier layer in the southeastern tropical
783 Indian Ocean. Journal of Geophysical Research: Oceans 110:.
784 https://doi.org/10.1029/2004JC002816

785 Rao RR (2003) Seasonal variability of sea surface salinity and salt budget of the mixed
786 layer of the north Indian Ocean. J Geophys Res 108:3009.
787 https://doi.org/10.1029/2001JC000907

788 Ren L, Riser SC (2009) Seasonal salt budget in the northeast Pacific Ocean. Journal of
789 Geophysical Research: Oceans 114:. https://doi.org/10.1029/2009JC005307

790 Saji N, Yamagata T (2003) Possible impacts of Indian Ocean Dipole mode events on
791 global climate. Clim Res 25:151–169. https://doi.org/10.3354/cr025151

792 Saji NH, Goswami BN, Vinayachandran PN, Yamagata T (1999) A dipole mode in the
793 tropical Indian Ocean. Nature 401:360–363. https://doi.org/10.1038/43854

794 Santoso A, McPhaden M, Cai W (2017) The defining characteristics of ENSO extremes
795 and the strong 2015/16 El Niño: ENSO extremes. Reviews of Geophysics 55:.
796 https://doi.org/10.1002/2017RG000560

797 Sprintall J, Révelard A (2014) The Indonesian Throughflow: Response to Indo-Pacific
798 climate variability. Journal of Geophysical Research: Oceans 119:.
799 https://doi.org/10.1002/2013JC009533

800 Sprintall J, Tomczak M (1992) Evidence of the barrier layer in the surface layer of the
801 tropics. Journal of Geophysical Research: Oceans 97:7305–7316.
802 https://doi.org/10.1029/92JC00407

803 Thompson B, Gnanaseelan C, Salvekar PS (2006) Variability in the Indian Ocean
804 circulation and salinity and its impact on SST anomalies during dipole events. J Mar
805 Res 64:853–880. https://doi.org/10.1357/002224006779698350

806 Vinayachandran PN, Nanjundiah RS (2009) Indian Ocean sea surface salinity
807 variations in a coupled model. Clim Dyn 33:245–263. https://doi.org/10.1007/s00382-
808 008-0511-6

809 Wijffels S, Meyers G (2004) An Intersection of Oceanic Waveguides: Variability in the
810 Indonesian Throughflow Region. Journal of Physical Oceanography - J PHYS
811 OCEANOGR 34:. https://doi.org/10.1175/1520-
812 0485(2004)034%253C1232:AIOOWV%253E2.0.CO;2

813 Xie S-P, Annamalai H, Schott FA, McCreary JP (2002) Structure and Mechanisms of
814 South Indian Ocean Climate Variability*. J Climate 15:864–878.
815 https://doi.org/10.1175/1520-0442(2002)015%253C0864:SAMOSI%253E2.0.CO;2

816 Xie S-P, Hu K, Hafner J, et al (2009) Indian Ocean Capacitor Effect on Indo–Western
817 Pacific Climate during the Summer following El Niño. Journal of Climate 22:730–747.
818 https://doi.org/10.1175/2008JCLI2544.1

819 Yang J, Liu Q, Xie S, et al (2007) Impact of the Indian Ocean SST basin mode on the
820 Asian summer monsoon. Geophysical Research Letters 34:2006GL028571.
821 https://doi.org/10.1029/2006GL028571

822 Yu L (2011) A global relationship between the ocean water cycle and near-surface
823 salinity. Journal of Geophysical Research: Oceans 116:.
824 https://doi.org/10.1029/2010JC006937

825 Zhang L, Han W, Meehl GA, et al (2021) Diverse impacts of Indian Ocean Dipole on
826 El Niño-Southern Oscillation. Journal of Climate 1–46. https://doi.org/10.1175/JCLI-
827 D-21-0085.1

828 Zhang N, Feng M, Du Y, et al (2016a) Seasonal and interannual variations of mixed
829 layer salinity in the southeast tropical Indian Ocean. J Geophys Res Oceans 121:4716–
830 4731. https://doi.org/10.1002/2016JC011854

831 Zhang Y, Du Y, Feng M (2018) Multiple Time Scale Variability of the Sea Surface
832 Salinity Dipole Mode in the Tropical Indian Ocean. Journal of Climate 31:283–296.
833 https://doi.org/10.1175/JCLI-D-17-0271.1

834 Zhang Y, Du Y, Qu T (2016b) A sea surface salinity dipole mode in the tropical Indian
835 Ocean. Clim Dyn 47:2573–2585. https://doi.org/10.1007/s00382-016-2984-z

836 Zhang Y, Du Y, Zheng S, et al (2013) Impact of Indian Ocean Dipole on the salinity
837 budget in the equatorial Indian Ocean: IOD INFLUENCE SALINITY BUDGET IN
838 EQIO. J Geophys Res Oceans 118:4911–4923. https://doi.org/10.1002/jgrc.20392

839 Zhang Z, Wang J, Yuan D (2022) Mixed Layer Salinity Balance in the Eastern Tropical
840 Indian Ocean. JGR Oceans 127:. https://doi.org/10.1029/2021JC018229

841 Zhu Q, Wang C (2024) Contributions of Indo-Pacific Forcings to Interannual
842 Variability of the Indonesian Throughflow in the Upper and Lower Layers. JGR Oceans
843 129:e2023JC020306. https://doi.org/10.1029/2023JC020306

844 Zuo H, Balmaseda MA, Tietsche S, Mogensen K, Mayer M (2019) The ECMWF
845 operational ensemble reanalysis–analysis system for ocean and sea ice: a description of
846 the system and assessment. Ocean Science15(3):779–808. https://doi.org/10.5194/os-
847 15-779-2019

848